PONTIFICIA UNIVERSIDAD CATÓLICA DEL PERÚ

Escuela de Posgrado

Quantitative ultrasound attenuation imaging for hepatic steatosis staging in bariatric patients: a pilot study

Tesis para obtener el grado académico de Maestro en Ingeniería Biomédica que presenta:

Christian Noé Soto Gálvez

Asesor:

*Roberto **Janniel** Lavarello Montero Ph.D.*

Lima, 2025

Informe de Similitud

Yo, Roberto Janniel Lavarello Montero, docente de la Escuela de Posgrado de la Pontificia Universidad Católica del Perú, asesor de la tesis titulada Quantitative ultrasound attenuation imaging for hepatic steatosis staging in bariatric patients: a pilot study, del autor Christian Noé Soto Gálvez, dejo constancia de lo siguiente:

- El mencionado documento tiene un índice de puntuación de similitud de 21%. Así lo consigna el reporte de similitud emitido por el software *Turnitin* el 12/01/2026.
- He revisado con detalle dicho reporte y la Tesis, y no se advierte indicios de plagio.
- Las citas a otros autores y sus respectivas referencias cumplen con las pautas académicas.

Lugar y fecha:
Lima, 12 de enero del 2026

Apellidos y nombres del asesor: Lavarello Montero, Roberto Janniel	
DNI:10544227	Firma
ORCID: 0000-0001-8472-5161	

Explicación sobre el índice de similitud de 21%:

El reporte incluye la bibliografía, la cual constituye 6 de las 44 páginas del documento, la cual ha sido casi íntegramente marcada por el software de análisis. Si dicha sección del documento no hubiese sido incluida, el porcentaje de similitud estaría muy por debajo del 20%, como se puede constatar del porcentaje ínfimo de texto resaltado en el cuerpo principal de la tesis.

Dedicado a mis padres, por su cariño y apoyo de siempre.
A mi hermana Karen, por impulsarme en cada paso.
A los profesores que me acompañaron en este camino.
A mis amigos y compañeros del LIM.

"All we have to decide is what to do with the time that is given us."
J. R. R. Tolkien

Acknowledgments

This thesis marks the culmination of my master's studies, and I am deeply grateful to my family for their loving support throughout this journey.

I extend my sincere gratitude to Professor Roberto Lavarello for welcoming me into the Laboratorio de Imágenes Médicas (LIM) and for his continued support throughout this work. His mentorship, trust, and encouragement were essential to the completion of this thesis. I also thank Professor Andrés Coila for his guidance and valuable feedback over the course of the project.

To my friends at LIM, thank you for the support, teamwork, and good times—working alongside you made the long days lighter and this experience truly memorable.

Finally, I would like to acknowledge the financial support that made this research possible. This work was funded by the Consejo Nacional de Ciencia, Tecnología e Innovación Tecnológica (CONCYTEC) through research grant No. PE501082070-2023-PROCIENCIA, which also allowed me to present part of my work at the 2025 IEEE International Ultrasonics Symposium in Utrecht, The Netherlands (IUS 2025).

Resumen

La evaluación fiable y no invasiva de la esteatosis hepática sigue siendo un reto en las poblaciones obesas, en las que la ecografía se ve limitada por las grandes profundidades de imagen, la reducción de la calidad de la señal y la variabilidad anatómica. Las imágenes cuantitativas de atenuación ecográfica ofrecen una vía fundamentada para la caracterización de los tejidos, pero su utilidad práctica depende de una estimación sólida a partir de datos in vivo obtenidos bajo consideraciones clínicas. Este trabajo presenta una evaluación piloto observacional de la estimación de la pendiente del coeficiente de atenuación (ACS) utilizando el método SWIFT (Spatially Weighted Fidelity and Regularization Terms for Attenuation Imaging) en pacientes bariátricos con histología como estándar de referencia. Los datos del canal de RF se obtuvieron utilizando una configuración de transductor convexo multifocal que admite profundidades de hasta 25 cm. Los mapas de ACS se calcularon en la vista de interfaz hepatorrenal, se calibraron con un maniquí de referencia y se resumieron los resultados utilizando valores medianos a nivel de paciente dentro de las regiones de interés (ROI) del parénquima hepático con ajustes de procesamiento preespecificados.

En 43 sujetos, la mediana del ACS a nivel de paciente aumentó con la severidad de la esteatosis, oscilando entre 0,530 dB/cm/MHz en S0 y 0,794 dB/cm/MHz en S3, con diferencias significativas entre los grados. Los análisis ROC exploratorios indicaron una separabilidad sustancial para las agrupaciones clínicamente relevantes (AUROC $> 0,86$), mientras que la validación cruzada «dejando-uno-fuera» mostró una variabilidad dependiente de la tarea en los puntos operativos basados en el índice de Youden, especialmente para la discriminación de grados inferiores, donde se espera un solapamiento entre grados adyacentes. Estos hallazgos respaldan el ACS basado en SWIFT como un marcador prometedor para clasificar la gravedad de la esteatosis en este entorno piloto, al tiempo que motivan la realización de estudios de validación más amplios con una calibración estructurada del ancho de banda utilizable y los parámetros del algoritmo, y referencias histológicas más cuantitativas para reducir la ambigüedad de la clasificación visual categórica.

Palabras clave: ultrasonido cuantitativo, pendiente del coeficiente de atenuación, imagen de atenuación ecográfica, esteatosis hepática.

Abstract

Reliable noninvasive assessment of hepatic steatosis remains challenging in obese populations, where ultrasound is constrained by large imaging depths, reduced signal quality, and anatomical variability. Quantitative ultrasound attenuation imaging offers a principled route to tissue characterization, but its practical utility depends on robust estimation from *in vivo* data acquired under clinical constraints.

This work presents an observational pilot evaluation of attenuation coefficient slope (ACS) estimation using the Spatially Weighted Fidelity and Regularization Terms for Attenuation Imaging (SWIFT) method in bariatric patients with histology as the reference standard. RF channel data were acquired using a multifocal convex-transducer configuration supporting depths up to 25 cm. ACS maps were computed in the hepatorenal interface view, calibrated with a tissue-mimicking reference phantom, and summarized using patient-level median values within liver parenchyma ROIs under pre-specified processing settings.

Across 43 subjects, patient-level median ACS increased with steatosis severity, ranging from 0.530 dB/cm/MHz in S0 to 0.794 dB/cm/MHz in S3, with significant differences across grades. Exploratory ROC analyses indicated substantial separability for clinically relevant groupings (AUROC > 0.86), while leave-one-out cross-validation showed task-dependent variability in Youden-index-based operating points, particularly for lower-grade discrimination where overlap between adjacent grades is expected. These findings support SWIFT-based ACS as a promising marker for ranking steatosis severity in this pilot setting, while motivating larger validation studies with structured calibration of the usable bandwidth and algorithm parameters, and more quantitative histological references to reduce ambiguity from categorical visual grading.

Keywords: quantitative ultrasound, attenuation coefficient slope, attenuation imaging, hepatic steatosis.

Table of Contents

List of Figures

List of Tables

Chapter 1

Introduction

Biomedical ultrasound is a noninvasive imaging modality based on the interaction of high-frequency sound waves with biological tissues through mechanisms such as scattering, absorption, and reflection, producing echo signals that contain information about the acoustic properties of the interrogated medium. Brightness (B-mode) imaging provides anatomical information based on the amplitude of backscattered signals, which depends on scatterer size, scatterer concentration, and variations of acoustic impedance within tissues. Despite its widespread use due to accessibility, this imaging mode remains fundamentally qualitative, device-dependent, and operator-dependent [1].

To overcome these limitations, Quantitative Ultrasound (QUS) adopts an approach based on the analysis of radiofrequency (RF) echo signals to characterize tissue properties related to microstructure, providing quantitative parameters that are not accessible through the conventional echogenicity of the B-mode image. By analyzing the spectral and statistical properties of backscattered ultrasound waves, QUS aims to derive reproducible biomarkers linked to intrinsic acoustic properties such as attenuation, scattering strength, speed of sound, and envelope statistics [2, 1].

Two commonly used parameters in QUS are the backscatter coefficient (BSC) and the attenuation coefficient slope (ACS). The BSC quantifies the scattering in the backward direction of the interrogated tissue and provides information related to the morphology and spatial distribution of the scatterers within the insonified region [2]. ACS describe the frequency dependent loss of acoustic energy as ultrasound propagates through tissue due to absorption and scattering mechanisms [3]. These parameters have been studied in a wide range of applications, including breast lesions, fatty liver disease, thyroid cancer [3], prostate cancer, micro metastases of lymph nodes [2], cell death [4], cervix ripening [5] and tumor response to therapy [6].

1.1 Clinical Motivation

Metabolic dysfunction–associated steatotic liver disease (MASLD) has become a major global public health concern, with a steadily increasing worldwide prevalence (30%) [7]. The prevalence rates are particularly high among individuals with excess body weight, reaching 69.99% in overweight populations and 75.27% in obese populations [8]. Liver biopsy is considered the gold standard method for assessing hepatic steatosis. Histologically, steatosis is commonly graded from 0 to 3 based on the proportion of hepatocytes containing macrovesicular fat: grade 0 ($< 5\%$), grade 1 (5–33%), grade 2 ($>$ 33–66%), and grade 3 ($> 66\%$) [9]. However, biopsy based assessment presents important drawbacks, including sampling variability, invasiveness, inconsistency between observers, and limited suitability for longitudinal monitoring [7]. These practical constraints have motivated the search for noninvasive alternatives that provide reproducible and quantitative assessments of hepatic fat.

In clinical practice, several noninvasive tests are used to provide scalable markers for the evaluation and follow-up of MASLD. Simple serum based scores, such as Fibrosis-4 (FIB-4), APRI, and the NAFLD Fibrosis Score (NFS), combine routinely available variables (e.g., age, aminotransferases, platelets) and are commonly used as first line tools due to their low cost and ease of implementation. However, their performance can be influenced by patient factors such as age and metabolic comorbidities, motivating recommendations to combine more than one noninvasive test when risk is intermediate or elevated [10]. In primary care settings, serologic steatosis calculators such as the Fatty Liver Index (FLI) and the Hepatic Steatosis Index (HSI) have also been proposed to identify individuals with suspected MASLD who may benefit from subsequent stratification of risk of fibrosis [11]. Although serum tests are inexpensive and widely available, they provide only indirect estimates of hepatic steatosis, exhibit limited accuracy to classify disease severity, and are highly susceptible to metabolic and demographic confounders, restricting their role primarily to risk stratification rather than quantitative assessment [10, 11, 12].

Beyond serology, magnetic resonance proton density fat fraction (MRI-PDFF) provides an imaging based quantitative estimate of hepatic fat content and has shown strong diagnostic performance for grading steatosis compared to biopsy. This method has high sensitivity and specificity in all steatosis thresholds, with excellent AUC values to discriminate normal from steatotic liver and to separate mild to moderate from more advanced steatosis grades, supporting MRI-PDFF as a robust noninvasive reference for hepatic fat quantification in MASLD [13]. MRI-based approaches are accurate, but remain constrained by cost and availability, sustaining interest in ultrasound based biomarkers that can be deployed more broadly.

1.2 Quantitative Ultrasound for Liver Tissue Characterization

Evaluation of hepatic steatosis based on ultrasound B-mode is performed reliably mainly in cases of moderate to severe fat infiltration and shows limited sensitivity to subtle changes or early stage disease [14]. QUS approaches have been introduced to address these limitations; however, their performance remains influenced by technical variability, acquisition conditions, and patient related factors. In particular, QUS methods rely on modeling assumptions regarding tissue homogeneity, diffraction, and scattering that are often violated in vivo, and their estimates are sensitive to acquisition settings, probe characteristics, and system dependent processing, leading to variability between platforms and clinical environments [1, 15, 2].

Attenuation based techniques, including Attenuation Imaging (ATI), Tissue Attenuation Imaging (TAI), and ultrasound guided attenuation parameter (UGAP), have demonstrated correlations with magnetic resonance imaging proton density fat fraction (MRI-PDFF) or biopsy in controlled cohorts [16, 17, 18, 19]. Despite these promising results, attenuation thresholds differ between systems and diagnostic performance varies substantially between patient populations. In cohorts with MASLD, attenuation coefficients often exhibit reduced sensitivity and considerable overlap between adjacent steatosis grades, particularly in the mild to moderate range, whereas higher discriminative performance has been reported in populations without MASLD [16].

The observed variability in attenuation based diagnostic performance arises from multiple sources of measurement variability and confounding. Attenuation estimates are strongly influenced by the placement of the region of interest (ROI), with degraded performance reported when ROIs are positioned too superficially or intersect reverberation artifacts [20, 21]. Vendors have also reported systematic decreases in attenuation values with increasing imaging depth, which complicates cross-platform standardization and limits reproducibility [22]. In addition, patient related factors such as body mass index, skin-to-capsule distance, and metabolic parameters contribute to inter-subject variability in attenuation measurements [17]. Together, these factors underscore the need for larger, well controlled validation studies to establish robust attenuation based biomarkers for clinical use [23, 24, 25, 26].

1.3 ACS Estimation Methods

Spectral based methods are widely used to estimate the ACS from pulse–echo RF data by exploiting the frequency dependent decay of the backscattered spectrum with depth. In particular, for the spectral log difference (SLD) method, ACS is ob-

tained from the log-ratio of power spectra computed in proximal and distal subwindows of an ROI under a linear frequency dependence assumption, but its practical use is limited by a strong tradeoff between spatial resolution and precision when estimates are computed independently per block [3]. Addressing this, the regularized spectral log difference (RSLD) framework reformulates ACS estimation as a 2-D inverse problem and introduces isotropic total variation (TV) priors on both the ACS map and the backscatter log difference term, improving spatial stability and extending the resolution variance tradeoff compared to blockwise SLD [3].

Recent work has focused on strengthening regularization by exploiting structure across the frequency dimension. A multi-frequency coupling approach using total nuclear variation (TNV) to jointly denoise spectral log ratio channels by leveraging shared structural information, reported fewer boundary artifacts and a higher contrast to noise ratio than single channel TV based denoising (TVSLD) in simulations, phantoms, and in vivo breast data [27]. In parallel, a regularized phantom-free ACS method aimed at reducing the dependence on calibrated reference media and improving robustness in homogeneous and heterogeneous tissues, although the method requires relatively large computing windows, which can compromise spatial resolution [28].

A key limitation of SLD derived attenuation imaging is performance degradation in the presence of moderate to large backscatter discontinuities, which can produce structured artifacts and compromise ACS maps. To address this limitation, the Spatially Weighted Fidelity and Regularization Terms (SWIFT) method introduces an inverse formulation specifically designed for media in which both attenuation and backscatter vary, directly targeting noise driven instability and interface related artifacts [29].

This issue is especially relevant in *in vivo* liver imaging, where intrahepatic vessels and parenchymal heterogeneity can introduce local backscatter discontinuities within candidate ROIs. Timaná et al. showed that such heterogeneity can bias attenuation and backscatter estimates and cannot always be eliminated by ROI placement alone [30]. This motivates evaluating SWIFT for *in vivo* liver ACS estimation, since its spatial weighting explicitly accounts for regions prone to discontinuities and may reduce bias near tissue interfaces [29].

1.4 Objectives

This study aims to demonstrate the feasibility of estimating the attenuation coefficient slope with the SWIFT method for hepatic steatosis assessment in bariatric patients, using liver biopsy as the reference standard.

Specific Objectives

1. To develop and deploy an in vivo hepatic acquisition protocol on a Verasonics Vantage NXT that enables multifocal transmission and RF channel data storage under clinical constraints.

2. To support ACS calibration for deep convex transducer acquisitions using a curved surface reference phantom with acoustic properties representative of healthy liver tissue.

3. To generate local ACS maps in the hepatorenal interface view from acquired RF ultrasound data using the SWIFT algorithm.

4. To derive patient level ACS summary metrics and quantify their association with biopsybased steatosis grades (S0–S3).

5. To explore the discriminative potential of ACS estimated with SWIFT for clinically relevant steatosis groupings (S$\geq$1, S$\geq$2, and S3) using receiver operating characteristic analysis and leave-one-out cross-validation.

1.5 Thesis Structure

This thesis is organized as follows.

Chapter 2, Ultrasound Scan Acquisition Setup, presents the ultrasound acquisition setup used in this work, including the system, the settings, and the data collection workflow.

Chapter 3, ACS Estimation Pilot Study, describes the application of the SWIFT method for ACS estimation and its evaluation for the classification of hepatic steatosis using liver biopsy as the reference standard.

Chapter 4, Results, presents the experimental findings, including group-wise comparisons between steatosis grades and diagnostic performance analyzes using cross-validation.

Chapter 2

Ultrasound Scans Acquisition Setup

Ultrasound liver scans were performed using a Verasonics Vantage NXT scanner (Redmond, WA, USA) with a C5-2v convex probe at Clínica Avendaño (Miraflores, Lima, Peru). Clínica Avendaño is a specialized bariatric surgery clinic that treats patients with an elevated body mass index (BMI) and increased abdominal circumference. This imposes practical constraints on ultrasound data acquisition to ensure adequate image quality, operator usability and acquisition reproducibility under clinical conditions.

1. A maximum imaging depth in the range of 20–25 cm to enable visualization of the liver parenchyma.
2. A real-time image buffer storing the most recent 10 frames, enabling retrospective selection of optimal imaging planes.
3. A single-action acquisition button, allowing simultaneous storage of sample data and the corresponding acquisition preset parameters.
4. Manual delineation of regions of interest (ROI), allowing the selection of the liver parenchyma.

2.1 Beam Geometry and Transmission Concepts

Focused transmission and multifocal imaging

Ultrasound imaging with array transducers commonly uses focused pulse transmission to concentrate acoustic energy at a selected depth. This is achieved by applying element dependent time delays so that emitted wavefronts constructively interfere at the focal region, improving lateral resolution and increasing the strength of the echo

signal near the focus [31]. A key limitation is that transmit focusing is inherently optimal only over a limited depth extent; away from the focal zone, the beam is still converging or already diverging, and lateral resolution degrades [31].

To extend good image quality over depth, conventional scanners often use multifocal (multi-zone) imaging, where multiple focused transmissions are emitted per image line using different focal depths, and the received data are combined into a single composite image [32]. This increases the depth range with improved lateral resolution, but at the cost of a reduced frame rate because several transmit events are required per line [32]. Although dynamic receiving focusing can maintain receiving side focusing across depths, transmit focusing remains tied to one focal depth per pulse [31], which is why multifocal transmission is still widely used in deep abdominal imaging.

f-number in ultrasound beamforming

In analogy to optical systems, the f-number of an ultrasound beam is defined as the ratio between the focal depth D and the effective aperture width A, such that $F = D/A$. This parameter provides a compact description of beam geometry and is directly related to lateral beamwidth and depth of field [31]. Smaller f-numbers, corresponding to larger apertures for a given depth, produce narrower beams with improved lateral resolution, whereas larger f-numbers result in wider beams with reduced lateral resolution but increased depth of field [31].

Reducing the f-number improves lateral resolution but confines optimal focusing to a more limited depth region, while larger f-numbers lead to more gradual beam divergence at the expense of lateral resolution, an effect that becomes more pronounced at greater imaging depths [33]. To balance this tradeoff, conventional beamforming strategies commonly employ a constant f-number approach, in which the active aperture is progressively increased with depth so that the focal ratio remains approximately constant [31]. This dynamic aperture strategy promotes a more uniform lateral beamwidth and a point spread function over depth.

In receive beamforming, a constant f-number is typically implemented by gradually including additional array elements as echoes arrive from increasing depths, until the full aperture is reached [34].

Walking aperture scanning

To form a two dimensional image using a one dimensional array, conventional focused ultrasound imaging relies on electronic scanning implemented through a walking aperture. In this approach, only a subset of adjacent transducer elements is activated for each transmit–receive event, defining a local active aperture that is

shifted laterally along the array to generate successive image lines [34]. For each transmission, the active sub aperture is centered at a different lateral position, such that the effective beam origin is stepped across the transducer aperture, producing a set of parallel or slightly steered beams without mechanical motion [34, 32].

By centering the active aperture around each beam position, the walking aperture strategy preserves symmetric focusing and a consistent beam geometry across the field of view. This prevents asymmetric beam profiles and focus errors that would arise if the entire array was used indiscriminately for all beam positions, particularly near the edges of the array [32]. In practice, the walking aperture is often combined with constant f-number beamforming, whereby the number of active elements is increased with depth to maintain comparable focusing conditions as the beam propagates deeper into the tissue [34].

2.2 System Configuration and Operation

The Verasonics Vantage NXT is a programmable research ultrasound platform that enables MATLAB based definition of custom transmit, receive sequences and acquisition presets, with access to radiofrequency channel data for offline processing [35, 36]. This flexibility allows for configuration of imaging timing, focusing strategies, and receive settings within a synchronized acquisition workflow.

Verasonics Vantage Configuration

For the present study, a multifocal transmission scheme was employed to ensure adequate image quality across the full imaging depth. Three individual memory buffer spaces were configured, corresponding to separate image reconstructions. For the real-time display shown in Fig. 2.2a, an intermediate data buffer was used to combine regions from each acquisition, resulting in a composite image that allowed the sonographer to select the optimal imaging view. For each maximum imaging depth, a corresponding set of focal depths was configured and a maximum frequency was selected by a practical rule [37], as shown in Table 2.1. A transmit f-number of 3.5 was selected for all focal configurations as a weakly focused transmit condition, consistent with previous quantitative ultrasound studies that employ f-numbers in the range of approximately 3–4 to balance lateral resolution and depth of field while preserving spectral stability for QUS estimation [38, 39]. No transmission apodization was configured.

A 16-bit variable was configured in the acquisition buffer, with 4096 samples per RF data column, following the Verasonics recommendations [36]. For each focal depth, 128 active elements were used in reception, and 128 transmit events were

Table 2.1: Multifocal transmission configurations used in the study.

Max. Img. Depth (cm)	Focal Depths (cm)	Central Freq. (MHz)
15	11, 8, 4	3.7
20	15, 9, 4	3.0
25	18, 12, 4	2.5

performed. With each transmission, a different array element was used as the center of the active aperture.

The total size of the acquisition buffer can be expressed as

$$S_{\text{bytes}} = \frac{N_{\text{bits}}}{8} \cdot N_{\text{samples}} \cdot N_{\text{Rx}} \cdot N_{\text{foci}} \cdot N_{\text{Tx}}, \tag{2.1}$$

where N_{bits} is the number of bits per sample, N_{samples} is the number of axial samples per RF data column, N_{Rx} is the number of active receive elements, N_{foci} is the number of focal depths and N_{Tx} is the number of transmit events.

For the presented configuration, $N_{\text{bits}} = 16$, $N_{\text{samples}} = 4096$, $N_{\text{Rx}} = 128$, $N_{\text{foci}} = 3$, and $N_{\text{Tx}} = 128$, that yielded

$$S_{\text{bytes}} = \frac{16}{8} \times 4096 \times 128 \times 3 \times 128 = 402{,}653{,}184 \text{ bytes}. \tag{2.2}$$

The resulting acquisition buffer size, computed using (2.1), was approximately 402 MB. Given the data size for every frame of the buffer, storing the whole buffer for each acquisition would significantly increase data transfer time and disrupt the clinical workflow. To maintain usability for the clinician and minimize acquisition latency, only a single frame was selected and stored from the rolling buffer of 10 frames at each acquisition event.

Control and Acquisition Module

To facilitate data acquisition and labeling by clinical staff, three graphical user interface (GUI) were implemented in MATLAB, to emulate the control workflows commonly found in commercial ultrasound scanners. As shown in Fig. 2.2, the Control and Acquisition module consists of three GUI, as follows:

1. **Initial Configuration Interface.** This interface is used at the start of each session to register the volunteer ID and select the maximum imaging depth from a predefined list, based on the volunteer's body habitus. A recommended transmit central frequency is suggested according to the selected depth, while allowing manual override when necessary. Once confirmed, these parameters are passed to the acquisition script so that all subsequent acquisitions within the session follow a consistent preset configuration.

(a) (b)

Figure 2.1: Clinical deployment of the ultrasound system. **(a)** Verasonics Vantage NXT system. **(b)** Clinical acquisition setup.

2. **Control and Acquisition Interface.** This interface provides real-time visualization of the ultrasound image and access to the main acquisition controls. It supports operator adjustment of gain compensation settings during scanning and enables navigation through a rolling cine buffer (10 frames) to retrospectively select the most suitable frame. To minimize acquisition latency and avoid workflow disruption due to data transfer, only a single user-selected frame is saved at each acquisition event rather than storing the full cine buffer. A single-action acquisition button allows storage of the selected frame together with the corresponding acquisition preset parameters required for offline image reconstruction. Additionally, the operator selects an acquisition view label from a predefined list to enforce consistent and identifiable file organization across subjects and scanning planes.

3. **ROI Selection Interface.** This interface is used offline during post-processing to manually delineate ROIs of liver parenchyma on the saved acquisitions. The interface allows the user to browse acquisitions organized by patient and acquisition view, visualize the corresponding B-mode image, and select the frame to annotate. ROIs can be delineated using polygonbased selections or rectangular ROIs. The stored ROI metadata are subsequently used to help generate spatial masks on the attenuation estimation grid, ensuring that quantitative ACS estimation is restricted to the intended liver parenchyma region.

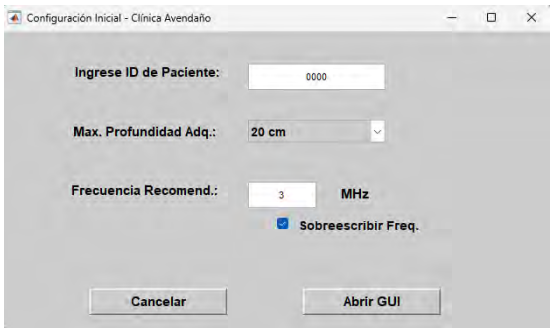

(a)

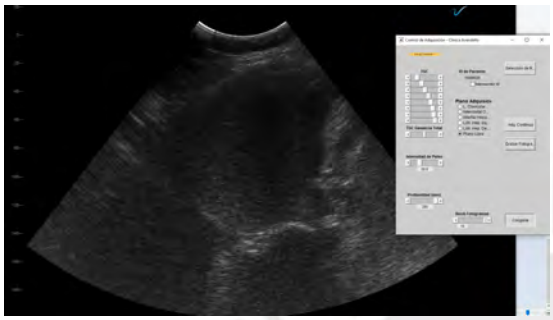

(b)

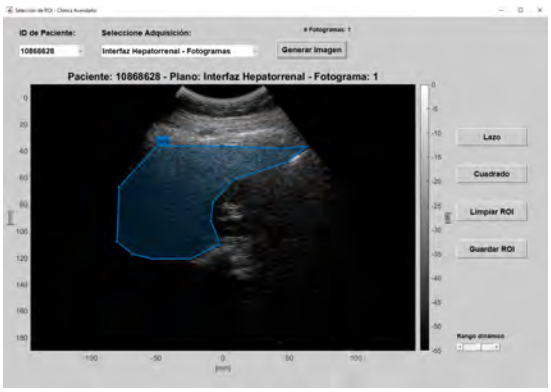

(c)

Figure 2.2: Graphical user interfaces used during data acquisition and processing. **(a)** Control and acquisition GUI. **(b)** ROI selection GUI. **(c)** Additional processing or visualization GUI.

2.3 QUS Phantom Especification

Several tissue-mimicking phantoms are available for purchase, however, most of the commercial ones are manufactured as a cylindrical or rectangular box with planar external surfaces, which is not suitable with the required imaging depths and the convex transducer footprint used in this study Therefore, a specific reference phantom was prepared and acoustically characterized for use as a reference.

This tissue-mimicking reference phantom was fabricated and acoustically characterized by the Quantitative Ultrasound Lab of the University of Wisconsin–Madison (Madison, WI, USA), with attenuation, backscatter coefficient, and speed of sound (SoS) properties designed to be representative of healthy liver tissue. The active volume was prepared using a variant of the tissue-mimicking material framework developed by Madsen et al. [40].

The phantom housing was manufactured as a rectangular enclosure with dimensions of 30 cm × 36 cm × 10 cm. The case was built from a 10 mm ABS sheet, and the scanning windows were fabricated using an aluminum multilayer composite to provide a durable acoustic interface for probe coupling.

Attenuation and SoS were measured using a through-transmission, narrowband technique with single-element transducers operated at 2.5, 3.5, 5, 7.5, and 10 MHz

(a) (b)

Figure 2.3: Tissue-mimicking reference phantom used in this study. (a) Overview of the phantom body. (b) Curved frontal interface with a convex array transducer placed in contact.

[41]. Measurements were performed at room temperatures between 21.65°C and 22.0°C, and precision was quantified as the standard deviation of five repeated measurements obtained by removing and replacing the sample in the acoustic path.

The phantom exhibits frequency-dependent attenuation following an approximately linear power law relationship over the 2.5–10 MHz range, with a mean specific attenuation of ∼0.524 dB/cm/MHz. The speed of sound is approximately constant across the measured bandwidth, with a mean value of ∼1535 m/s at room temperature.

Backscatter coefficient measurements were performed using a pulse–echo, broadband technique [42]. For each frequency band, BSC estimates were obtained at 64 spatially distinct locations within the phantom. Frequency dependent mean BSC values were computed across locations, and measurement precision was quantified using 95% confidence intervals calculated as ±1.96 times the standard deviation. Mean BSC values increased with frequency, with band averaged values of approximately 3×10^{-5} to 5×10^{-4} $\mathrm{cm}^{-1}\mathrm{sr}^{-1}$ (1.8–3.8 MHz), 2×10^{-4} to 5×10^{-3} $\mathrm{cm}^{-1}\mathrm{sr}^{-1}$ (3–8 MHz), and 1×10^{-3} to 1×10^{-2} $\mathrm{cm}^{-1}\mathrm{sr}^{-1}$ (4.9–14.9 MHz).

Fig. 2.3 shows the tissue-mimicking reference phantom used in this work. The curved frontal surface facilitates acoustic coupling with convex array transducers, avoiding interface mismatch relative to conventional planar phantoms and accommodating the transducer footprint used in the acquisitions.

2.4 On the acquisition setup and channel data

The specification of the reference phantom to match healthy liver acoustic properties helps ensure representative acquisition and processing conditions. Appropriate attenuation supports realistic signal decay for attenuation compensation and ACS estimation, a similar speed of sound reduces beamforming mismatch under a fixed speed of sound assumption, and a comparable backscatter coefficient yields RF amplitudes in the same range as in vivo data, helping avoid signal saturation.

Beyond supporting stable real-time imaging, the acquisition configuration and graphical user interfaces implemented in this work were designed to facilitate clinical scanning in a wide range of body habitus, including cases where probe positioning and depth selection are challenging. The use of predefined acquisition parameters helped standardize data acquisition for clinical operators without requiring manual beamforming adjustments during scanning. This configuration prioritizes operator usability and standardized acquisition while preserving access to RF channel data for posterior processing.

The storage of raw channel data preserves access to the measured transmit–receive signals for retrospective processing. Although focused transmissions with a walking aperture do not explicitly acquire a complete multistatic dataset, it has been shown that the complete multistatic response can be recovered from such acquisitions using retrospective encoding and model based inversion techniques, including REFoCUS and its regularized extensions [43, 44]. These formulations account for the transmit delays and apodization associated with focused and walking aperture sequences, enabling reconstruction of analogous multistatic data from standard clinical acquisitions.

The availability of channel data therefore allows for beamforming under alternative imaging models and supports advanced post-processing methods that rely on multistatic information, including sound speed estimation and aberration correction frameworks [34, 45].

Chapter 3

ACS MASLD Grading Pilot Study

An observational pilot study was conducted to evaluate whether SWIFT based ACS estimation can be implemented reliably *in vivo* in bariatric patients, using liver biopsy as the reference standard. The emphasis was an end-to-end of the acquisition/processing pipeline under prespecified parameters, while associations with histological grade and ROC-based separability were examined as exploratory evidence to inform future validation.

Given the limited prior information typical of early stage studies, the sample size was chosen to support protocol operability and obtain preliminary parameter estimates rather than to provide formal power for clinical validation. Published guidance commonly recommends on the order of ∼12 participants per group for pilot studies [46], and stepped rules for external pilots with continuous outcomes suggest ∼10–15 participants per group for medium to large anticipated effects, with a lower bound of 10 per group to preserve core pilot objectives [47]. Based on these considerations and the expected grade distribution in the bariatric cohort, the study aimed for approximately 10 subjects per steatosis grade.

3.1 Spatially Weighted Fidelity and Regularization Terms for Attenuation Imaging (SWIFT)

Spatially Weighted Fidelity and Regularization Terms for Attenuation Imaging (SWIFT) is a quantitative ultrasound method proposed to improve local ACS estimation in heterogeneous media where both attenuation and backscatter vary spatially [29]. The method is based on the regularized spectral log difference (RSLD) framework [3] and addresses its limitations at tissue interfaces.

In the SLD formulation, the logarithmic spectral ratio at spatial location (i, j)

and frequency f_k is modeled as

$$Y_{i,j,k} = 4L\,\beta_{i,j} f_k + c_{i,j} + \eta_{i,j,k}, \tag{3.1}$$

where L is the axial separation between the analysis windows, $\beta_{i,j}$ denotes the local attenuation coefficient slope, $c_{i,j}$ represents the logarithmic difference of backscatter coefficients between the proximal and distal windows, and $\eta_{i,j,k}$ is additive noise.

By stacking all measurements, the forward model can be written in matrix form as

$$\mathbf{y} = \mathbf{A}\mathbf{x} + \boldsymbol{\eta}, \tag{3.2}$$

with $\mathbf{x} = [\boldsymbol{\beta}^\top \ \mathbf{c}^\top]^\top$ containing the ACS and backscatter log difference maps.

The RSLD method imposes a total variation (TV) regularization on both $\boldsymbol{\beta}$ and $\mathbf{c}$ to stabilize the inverse problem. However, as shown in [29], the assumption of piecewise smoothness for the backscatter term $\mathbf{c}$ is frequently violated in heterogeneous tissue, where backscatter changes tend to be localized and abrupt. This mismatch leads to artifacts in the estimated ACS, specially near tissue interfaces.

SWTV-ACE introduced spatial weighting to the regularization of the backscatter related term to mitigate this effect [48]. Although effective when backscatter variations dominate, this approach does not modify the data fidelity term and, therefore, remains sensitive when attenuation and backscatter vary simultaneously.

SWIFT introduces two key modifications to the RSLD framework [29]. First, the backscatter log difference term is regularized using an ℓ_1-norm,

$$\|\mathbf{c}\|_1, \tag{3.3}$$

which promotes sparsity and reflects the localized nature of backscatter discontinuities. Second, SWIFT incorporates spatially varying weights into both the fidelity and regularization terms, yielding the optimization problem

$$\hat{\mathbf{x}} = \arg\min_{\boldsymbol{\beta},\mathbf{c}} \frac{1}{2} \left\|\mathbf{W}_f \left(\mathbf{y} - \mathbf{A}\mathbf{x}\right)\right\|_2^2 + \mu_b \mathrm{TV}(\boldsymbol{\beta}) + \mu_c \left\|\mathbf{W}_r \mathbf{c}\right\|_1 . \tag{3.4}$$

Where, $\mathbf{W}_f$ is a spatial weighting matrix applied to the data fidelity term, and $\mathbf{W}_r$ is a spatial weighting matrix applied to the sparsity constraint on $\mathbf{c}$. Both weighting matrices are derived from an initial unweighted reconstruction, using the estimated backscatter log difference map to identify regions where the assumptions of the SLD model are likely violated.

Compared with RSLD, SWIFT replaces smoothness based regularization of the backscatter term with a sparsity promoting prior and introduces spatial weighting in the fidelity term, reducing the influence of spectral measurements corrupted by

backscatter heterogeneity [29]. In contrast to SWTV-ACE, which applies spatial weighting only to the regularization of the backscatter related term, SWIFT additionally weights the data fidelity term itself. This distinction is shown to be critical when attenuation and backscatter variations coexist, leading to improved error and contrast to noise ratio performance in simulations, phantoms and in vivo samples [29, 48].

3.2 Ultrasound Acquisition Protocol

Patients are initially scheduled for bariatric surgery with a laparoscopic liver biopsy performed as part of their treatment. From this cohort, volunteers were recruited to undergo ultrasound examinations, provided no medical contraindications by the attending physician were found.

The day after the surgical procedure, ultrasound scans were acquired; during this period, volunteers are on a clear liquid diet, as part of their post-procedure recovery process. Scans were conducted with the patient lying down in the supine position with the right arm abducted behind the head to improve the acoustic window and increase the intercostal spacing.

Six ultrasound scan planes were acquired for each volunteer, as in (i) Midclavicular line, (ii) Oblique intercostal line inferior axillary line, (iii) Hepatorenal interface, (iv) Left hepatic lobe, (v) Right hepatic lobe, and (vi) a Free plane selected at the discretion of the sonographer.

3.3 ACS Estimation

For the purposes of this study, the analysis was restricted to the hepatorenal interface (HRI) view. This choice provided a standardized anatomical configuration across subjects and reduced variability related to acquisition plane selection and body habitus. The HRI view was selected due to its anatomical clarity, as the renal cortex provides a consistent landmark that facilitates the identification of the liver parenchyma. A rectangular region of interest (ROI) was manually defined to maximize the inclusion of the liver parenchyma while maintaining a geometry compatible with blockwise spectral analysis. Then a binary spatial mask was defined on the attenuation estimation grid to isolate liver parenchyma only, and all attenuation estimates, statistical analyzes, and visualizations were restricted to pixels within this mask.

ACS maps were estimated using the SWIFT method. Local power spectra were computed using overlapping analysis blocks with an 80% overlap. Estimation was performed in the polar domain using blocks spanning 12 adjacent scanlines laterally

and 15 wavelengths axially (9.24 mm). These window sizes were empirically selected as the smallest values expected to yield stable spectral estimates while preserving spatial resolution, and then kept fixed across all subjects to ensure a consistent configuration; these dimensions are broadly consistent with the axial and lateral resolutions recommended for backscatter coefficient estimation [49].

The frequency range for the estimation of ACS for this cohort was restricted to [1.5, 3.5] MHz. This bandwidth was selected empirically by inspecting the power spectra of the analyzed image regions and identifying the -20 dB limits that defined the lower and upper bounds, following a procedure similar to that described by Merino and Lavarello [29]. The regularization parameters were fixed for all samples ($\mu_b = 10^3$, $\mu_c = 10^1$) after an initial empirical tuning on a subset of cases to achieve stable ACS maps without overregularization. These values are of comparable magnitude to those reported in [29], and all processing settings were kept constant across subjects to avoid case specific adjustment.

3.4 Statistical analysis

An exploratory analysis was conducted to examine the association between ACS derived metrics and biopsy based steatosis grade in this pilot cohort. All analyzes were performed using the patient level median value of the SWIFT-derived ACS map.

Descriptive statistics

Attenuation values were summarized using the median and interquartile range (Q1–Q3) for each grade of steatosis (S0–S3). These descriptive statistics were used to characterize the distribution of attenuation values across grades and to support subsequent group-wise comparisons.

Group-wise comparison

Differences in attenuation values among steatosis grades were explored using the non-parametric Kruskal–Wallis test. This test was selected due to the limited sample size and the absence of distributional assumptions. Before hypotesis testing, group sizes, dispersion, and the presence of ties were examined to confirm suitability for the test. Statistical significance was defined as $p < 0.05$.

Receiver operating characteristic analysis

The discriminative performance of ACS for clinically relevant steatosis groupings was explored using receiver operating characteristic (ROC) analysis under the Kleiner grading system (S0–S3). Three binary classification tasks were considered to reflect commonly used clinical thresholds: (i) S$\geq$1 vs. S0, assessing the presence of any steatosis versus none; (ii) S$\geq$2 vs. S$\leq$1, separating moderate-to-severe steatosis from mild or absent disease; and (iii) S3 vs. S$\leq$2, isolating severe steatosis from all lower grades. For each task, ROC curves were constructed and the area under the ROC curve (AUROC) was computed as a measure of separability.

For a given decision threshold T, sensitivity and specificity were quantified through the true positive rate (TPR) and false positive rate (FPR), defined as

$$\mathrm{TPR}(T) = \frac{\mathrm{TP}(T)}{\mathrm{TP}(T) + \mathrm{FN}(T)}, \qquad \mathrm{FPR}(T) = \frac{\mathrm{FP}(T)}{\mathrm{FP}(T) + \mathrm{TN}(T)}. \tag{3.5}$$

A Youden-based operating point was used to summarize the sensitivity–specificity trade-off by maximizing Youden's index,

$$J(T) = \mathrm{TPR}(T) - \mathrm{FPR}(T), \tag{3.6}$$

and the corresponding sensitivity and specificity were reported. These operating points are cohort-specific and are not intended as definitive clinical decision thresholds.

Given the limited cohort size, leave-one-out cross-validation was used to obtain an internal estimate of out-of-sample discriminative performance and to examine operating point stability. In each iteration, one subject was excluded, and the Youden-based operating point was determined using the remaining data via ROC analysis. The resulting threshold was then applied to the excluded subject to obtain an out-of-sample classification. After iterating over all subjects, sensitivity and specificity were derived from the resulting confusion matrix. The variability of the thresholds across folds was additionally analyzed as an indicator of cutoff stability.

Chapter 4

Results

4.1 ACS Estimation Maps

Attenuation coefficient slope maps were obtained using the SWIFT method for all acquisitions. Fig. 4.1 shows representative ACS maps across steatosis grades S0–S3.

In the representative cases shown, ACS maps present spatially smooth distributions within the liver ROI under the fixed processing settings, with anatomically plausible attenuation patterns and no gross artifacts within the analyzed region. Lower-grade examples exhibit lower attenuation values with moderate variability within the parenchyma, whereas higher-grade examples show more extended regions of elevated attenuation while maintaining smooth axial trends. These examples also illustrate an increase in median ACS with steatosis grade, together with the presence of spatial heterogeneity within individual acquisitions.

4.2 Statistical Results

A total of $N = 43$ subjects with valid attenuation estimates and histological classification were included in the analysis. The cohort spanned all histological grades of steatosis with the following distribution: S0 ($n = 13$), S1 ($n = 8$), S2 ($n = 15$), and S3 ($n = 7$). Across subjects, ACS values ranged from 0.392 to 0.979 dB/cm/MHz, with a cohort median of 0.652 dB/cm/MHz and an interquartile range (IQR) of 0.571–0.782 dB/cm/MHz.

Patient level median ACS values increased with steatosis grade (Fig. 4.2). Adjacent grades showed interquartile overlap, most notably for S0–S1 and S1–S2, with comparatively reduced overlap for S2–S3. This behavior is consistent with within grade variability expected from the broad histological fat fraction ranges defining S1–S3 (5–33%, 33–66%, and >66%, respectively). In addition, variability in S0 may be influenced by increased visibility of intrahepatic vascular structures and

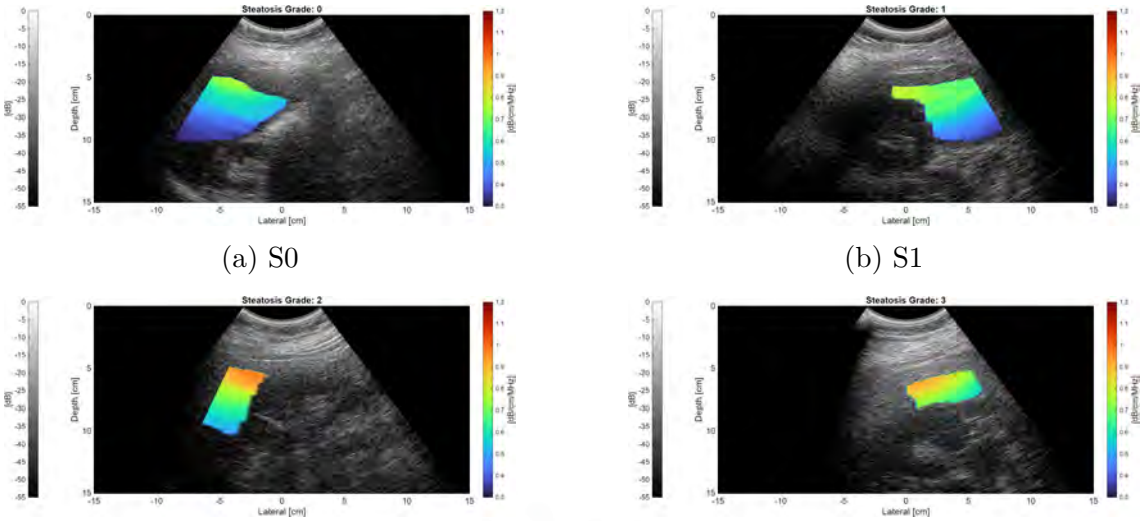

(a) S0 (b) S1

(c) S2 (d) S3

Figure 4.1: Representative ACS maps for each steatosis grade. Median ACS values are S0 = 0.539, S1 = 0.644, S2 = 0.732, and S3 = 0.769 dB/cm/MHz.

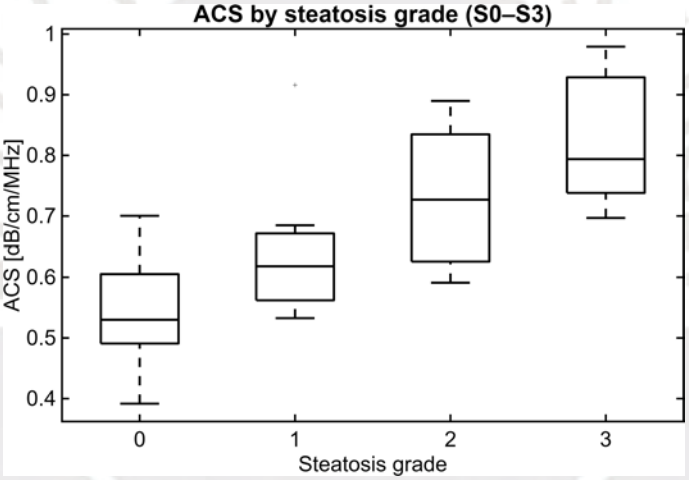

Figure 4.2: Distribution of patient level median ACS values stratified by histological steatosis grade (S0–S3).

other tissue components in low fat livers, which can increase apparent parenchymal heterogeneity compared to steatotic cases where such structures are progressively obscured in B-mode imaging [30].

Table 4.1 summarizes the median and interquartile range (Q1–Q3) of the distribution of the attenuation coefficient for each grade of steatosis.

Group comparison across grade of steatosis

Before hypothesis testing, attenuation distributions were examined for group size adequacy and dispersion comparability. The dispersion was similar across grades, with maximum to minimum ratios of 1.91 for the interquartile range and 1.85 for the median absolute deviation.

Table 4.1: Summary of patient level median attenuation coefficient slope by steatosis grade.

Steatosis grade	Median (dB/cm/MHz)	Q1 (dB/cm/MHz)	Q3 (dB/cm/MHz)	N
S0	0.530	0.491	0.605	13
S1	0.618	0.562	0.671	8
S2	0.727	0.626	0.835	15
S3	0.794	0.738	0.929	7

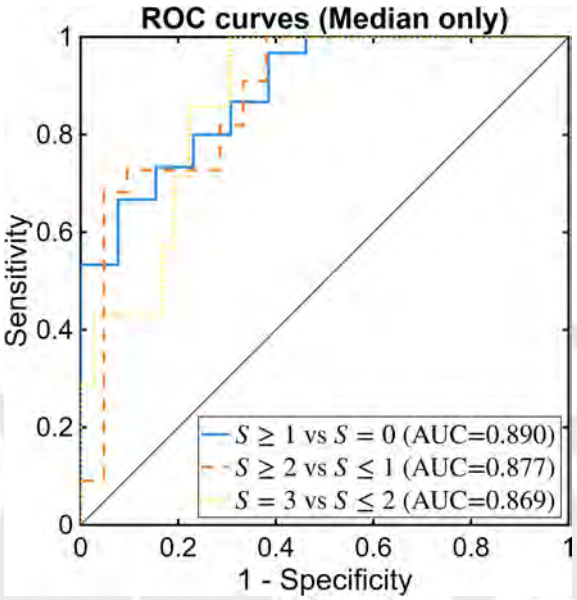

Figure 4.3: ROC curves for steatosis stage discrimination by attenuation coefficient.

Group differences in patient level median ACS between steatosis grades S0–S3 were evaluated using the non-parametric Kruskal–Wallis test, which indicated a statistically significant difference accross grades ($p < 0.001$).

Diagnostic performance analysis

ROC analysis was used to explore separability of the patient level median ACS for three clinically relevant classification tasks (S≥1 vs. S0, S≥2 vs. S≤1 and S3 vs. S≤2). Summary metrics are reported in Table 4.2, and the corresponding ROC curves are shown in Fig. 4.3. In all tasks, the AUROC values exceeded 0.86, indicating substantial separability in this cohort. The sensitivity–specificity tradeoff varied by task, with higher specificity for lower-grade thresholds and higher sensitivity for identifying severe steatosis.

Out-of-sample classification performance

Leave-one-out cross-validation (LOOCV) was used to obtain an internal estimate of threshold-based classification behavior under fold specific training data. In each fold,

Table 4.2: Performance metrics for attenuation coefficient in steatosis grading (S0–S3).

	In-sample				LOOCV	
Comparison	**AUC**	**Threshold**	**Sens.**	**Spec.**	**Sens.**	**Spec.**
S≥1 vs. S0	0.890	0.658	0.667	0.923	0.667	0.615
S≥2 vs. S≤1	0.877	0.721	0.682	0.952	0.636	0.619
S3 vs. S≤2	0.869	0.697	1.000	0.694	0.857	0.695

* Threshold values are expressed in dB/cm/MHz.

Table 4.3: Row-normalized confusion matrices (%) from LOOCV using attenuation coefficient. Percentages are normalized by true class.

Comparison	True class	Predicted class (%)					
		S≥1 vs S0		S≥2 vs S≤1		S3 vs S≤2	
		Pos.	Neg.	Pos.	Neg.	Pos.	Neg.
	Pos.	66.7	33.3	63.6	36.4	85.7	14.3
	Neg.	38.5	61.5	38.1	61.9	30.6	69.4

the decision threshold was determined using only the training subset, resulting in fold dependent operating points that differed across tasks. For S≥1 vs. S0, thresholds ranged from 0.555 to 0.658 dB/cm/MHz, while for S≥2 vs. S≤1, thresholds ranged from 0.591 to 0.721 dB/cm/MHz. In contrast, the thresholds for S3 vs. S≤2 were tightly clustered around 0.697 dB/cm/MHz.

Row-normalized confusion matrices summarizing LOOCV results are shown in Table 4.3. Normalization by the true class was used to account for class imbalance and to facilitate interpretation in terms of sensitivity and specificity. For discrimination between S≥1 and S0 (30 vs. 13 patients), errors were predominantly false positives near the normal–steatosis boundary, consistent with overlap between S0 and S1 attenuation values and with within-grade variability given the broad fat fraction range defining mild steatosis (5–33%). For discrimination between S≥2 and S≤1 (22 vs. 21 patients), errors were more evenly distributed between false positives and false negatives, consistent with partial separation between adjacent grades.

The most consistent cross-validated behavior was observed for discrimination of severe steatosis (S3 vs. S≤2; 7 vs. 36 patients), which showed minimal threshold variability across folds and high sensitivity, suggesting increased separability at more advanced disease stages.

4.3 Discussion

In this pilot cohort, patient level ACS values increased from S0 to S3, consistent with the expected biophysical relationship between hepatic fat accumulation and ultrasound attenuation. Grade-wise median values fell within ranges reported in prior histology referenced work by Ormachea and Parker [50], supporting that the implemented acquisition configuration and calibration/processing workflow yielded attenuation estimates on a physiologically plausible in vivo scale. At the same time, ACS distributions showed partial overlap between adjacent grades, most notably for early-stage disease, which is consistent with biological variability and with the broad fat-fraction ranges defining histological grades (S1: 5–33%, S2: 33–66%, S3: >66%), leading to subjects near bin boundaries that can be attenuation-similar.

Similar monotonic trends have been reported across attenuation-based techniques, including ATI/TAI-derived metrics. Although absolute attenuation values and operating points vary between studies due to differences in acquisition protocols, transducer characteristics, calibration, and processing pipelines, the grade-wise ordering observed in this work is consistent with the literature. A comparative summary of attenuation values and reported diagnostic metrics reported in previous studies is provided in Table 4.4.

Discriminative performance and operating points

ROC analysis indicated that patient level median ACS provides consistent ranking across the evaluated steatosis classification tasks. This suggests that ACS captures systematic differences between histological stages in this cohort, which is consistent with prior histology-referenced attenuation imaging studies.

For threshold-based use, an operating point must be selected. Here, in-sample operating points were summarized using Youden's index and are reported as cohort-specific reference values rather than definitive clinical cutoffs.

Threshold behavior and class imbalance

Leave-one-out cross-validation suggested task-dependent differences in operating-point stability. For lower-grade discrimination tasks ($S \geq 1$ vs. S0 and $S \geq 2$ vs. $S \leq 1$), fold-specific thresholds varied substantially, consistent with attenuation overlap near early clinical boundaries and with within-grade variability introduced by broad histological fat-fraction ranges (e.g., S1: 5–33%, S2: 33–66%). In this regime, small perturbations in the training set can shift the Youden-selected operating point without materially changing ranking performance, yielding non-unique near-optimal thresholds.

In contrast, discrimination of severe steatosis (S3 vs. S$\leq$2) showed tightly clustered thresholds across folds. This behavior is consistent with increased separability at advanced disease stages together with pronounced class imbalance. Because S3 cases occupy a higher ACS range and represent a small minority of the cohort, an operating point that prioritizes sensitivity for severe steatosis can remain relatively stable while tolerating a moderate number of false positives in the larger S$\leq$2 group. As a result, the Youden-based threshold for S3 discrimination can occur at a lower value than that for S$\geq$2 discrimination, despite the monotonic increase of ACS with disease severity.

In-sample versus cross-validated classification behavior

In-sample and cross-validated analyses differed primarily in threshold-dependent behavior, particularly for specificity in lower-grade classification tasks. This reflects the fact that ROC-based ranking can remain relatively consistent even when the threshold selected by Youden's index varies across resampling folds.

These observations highlight the distinction between ranking-based discrimination and threshold-based classification in small pilot cohorts. While ACS provides separability between steatosis groupings, the operating point is sensitive to overlap near grade boundaries, class imbalance, and limited sample size. These factors should be considered when translating exploratory operating points into clinically actionable thresholds, especially for early-stage disease.

Table 4.4: Comparison of attenuation-based steatosis discrimination performance with values reported in the literature. Differences in reference standard and device-specific scaling should be considered when interpreting cut-offs.

Study	Reference standard	Task definition	AUC	Cut-off	Sens.	Spec.
This work (in-sample)	Histology (S0–S3)	S≥1 vs S0	0.890	0.658	0.666	0.923
		S≥2 vs S≤1	0.877	0.721	0.682	0.952
		S3 vs S≤2	0.869	0.697	1.000	0.694
Hsu et. al ([51])	Histology (S0–S3)	S≥1 vs S0	0.970	0.69*	1.00	0.830
		S≥2 vs S≤1	0.990	0.78*	1.00	0.900
		S3 vs S≤2	0.970	0.84*	1.00	0.850
Sugimoto et. al ([20])	Histology (S0–S3)	S≥1 vs S0	0.750	0.67	–	–
		S≥2 vs S≤1	0.824	0.72	–	–
		S3 vs S≤2	0.849	0.86	–	–
Li et. al ([16])	Histology (S0–S3)	S≥1 vs S0	0.836	0.790	0.844	0.823
		S≥2 vs S≤1	0.774	0.88	0.802	0.682
		S3 vs S≤2	0.688	0.93	0.727	0.638
Jeon et. al ([19])	MRI-PDFF	PDFF ≥5%	0.861	0.884	0.780	0.789
		PDFF ≥10%	0.835	0.980	0.644	0.934
Fan et. al ([23])	CAP (>250 dB/m)	S≥1 vs S0	0.876	0.93	0.671	0.956
		S≥2 vs S≤1	0.848	0.95	0.756	0.805
		S3 vs S≤2	0.835	0.99	0.723	0.803

*Cut-offs rescaled following the unit convention explicitly stated in the cited study.

4.4 Limitations and future work

This work was designed as a pilot evaluation under a single acquisition configuration and a cohort-specific empirical bandwidth selection. ACS estimation was evaluated using a fixed and consistent set of processing parameters: empirically well behaved values for the usable frequency band and SWIFT regularization parameters were selected based on preliminary inspection and previous reported values and then held constant across all subjects to ensure reproducibility. Future work should include a structured calibration and optimization of the usable frequency band and SWIFT hyperparameters across acquisition settings to better characterize robustness and generalizability beyond the present pilot conditions.

An additional limitation relates to the ultrasound acquisition protocol. Scans were performed in the early postoperative period after bariatric surgery, as local clinical practice required confirmation of laparoscopic liver biopsy prior to volunteer participation. Although this ensured histological reference availability, postoperative discomfort limited the volunteers' ability to take deep or sustained breath holds, constraining the optimization of the acoustic window. As a result, rib shadowing and reduced image quality were observed in this cohort, particularly in deep abdominal views. Addressing this will require evaluation of alternative acquisition protocols, including preoperative or delayed postoperative scanning, to improve image quality while minimizing disruption to clinical workflow.

ACS estimation also remains ROI dependent. Although SWIFT mitigates moderate backscatter variability, strong interfaces and rib shadowing can distort local spectra and bias estimates, highlighting the need for ROI quality control and automated exclusion of shadowed or interface adjacent regions.

In addition, histological steatosis grading is reported in broad categorical bins (e.g., S0: 0–5%) and is typically based on visual assessment, which can introduce reader-dependent variability and occasional borderline calls when used as a reference for continuous imaging biomarkers. Incorporating quantitative histology would provide a continuous reference standard and help adjudicate cases near grade boundaries. As illustrated in Fig. 4.4, two biopsies labeled as S0 can show markedly different degrees of visible lipid vacuolization, suggesting that categorical visual grading may not fully capture the underlying fat fraction in all cases and is subject to inter-reader variability.

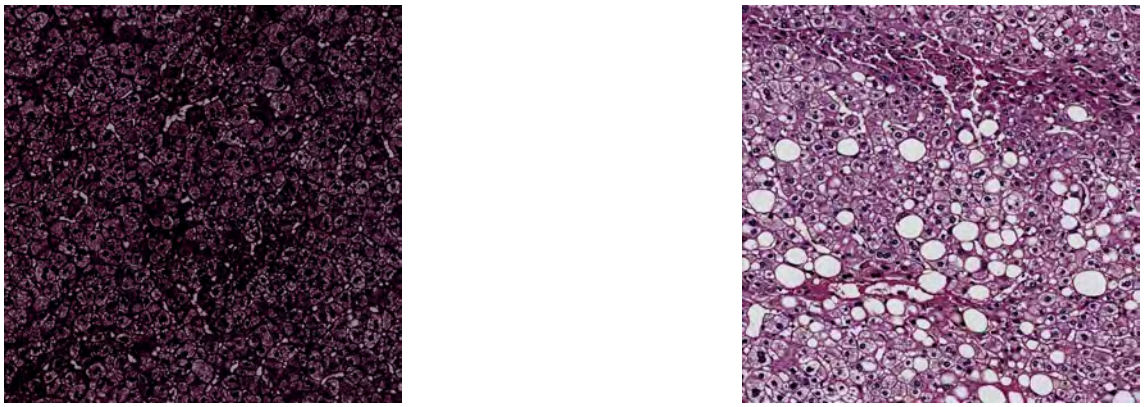

(a) (b)

Figure 4.4: Representative histology examples labeled as Grade 0 (S0). (a) Example consistent with minimal lipid vacuoles. (b) Example also labeled as S0, showing a noticeably higher presence of lipid vacuoles.

Finally, larger prospective cohorts will be required to obtain more precise estimates of variability and cross-validated performance, and to support clinically interpretable operating-point selection under class imbalance and grade overlap.

Chapter 5

Conclusions

This work implemented an end-to-end pipeline for SWIFT-based attenuation coefficient slope estimation in vivo in a bariatric cohort with histology as the reference standard, demonstrating practical acquisition, processing, and patient-level summarization under pre-specified settings. The resulting ACS values exhibited a monotonic increase with steatosis grade and fell within ranges previously reported in histology-referenced studies, supporting a physiologically plausible attenuation scale under the study acquisition conditions.

Exploratory ROC analyses indicated substantial separability for clinically relevant steatosis groupings, reflecting robust ranking behavior across tasks. In contrast, threshold-based classification showed task-dependent behavior: operating points for lower-grade discrimination were more sensitive to overlap and cohort composition, whereas severe steatosis discrimination exhibited more consistent cross-validated behavior and reduced operating-point variability.

In general, these findings support SWIFT-based ACS as a promising quantitative marker for ranking steatosis severity in this pilot setting, while highlighting that threshold selection is cohort-dependent and requires larger, dedicated validation studies before clinical cutoffs can be defined.

Bibliography

[1] G. Cloutier, F. Destrempes, F. Yu, and A. Tang, "Quantitative ultrasound imaging of soft biological tissues: a primer for radiologists and medical physicists," 12 2021.

[2] M. L. Oelze and J. Mamou, "Review of quantitative ultrasound: Envelope statistics and backscatter coefficient imaging and contributions to diagnostic ultrasound," 2 2016.

[3] A. L. Coila and R. Lavarello, "Regularized spectral log difference technique for ultrasonic attenuation imaging," *IEEE Transactions on Ultrasonics, Ferroelectrics, and Frequency Control*, vol. 65, pp. 378–389, 3 2018.

[4] A. Sadeghi-Naini, O. Falou, H. Tadayyon, A. Al-Mahrouki, W. Tran, N. Papanicolau, M. C. Kolios, and G. J. Czarnota, "Conventional frequency ultrasonic biomarkers of cancer treatment response in vivo," *Translational Oncology*, vol. 6, pp. 234–IN2, 6 2013.

[5] Q. W. Guerrero, H. Feltovich, I. M. Rosado-Mendez, L. C. Carlson, and T. J. Hallcor, "Quantitative ultrasound biomarkers based on backscattered acoustic power: Potential for quantifying remodeling of the human cervix during pregnancy," *Ultrasound in Medicine & Biology*, vol. 45, pp. 429–439, 2 2019.

[6] K. Quiaoit, D. DiCenzo, K. Fatima, D. Bhardwaj, L. Sannachi, M. Gangeh, A. Sadeghi-Naini, A. Dasgupta, M. C. Kolios, M. Trudeau, S. Gandhi, A. Eisen, F. Wright, N. Look-Hong, A. Sahgal, G. Stanisz, C. Brezden, R. Dinniwell, W. T. Tran, W. Yang, B. Curpen, and G. J. Czarnota, "Quantitative ultrasound radiomics for therapy response monitoring in patients with locally advanced breast cancer: Multi-institutional study results," *PLOS ONE*, vol. 15, p. e0236182, 7 2020.

[7] D. Hudson, T. Afzaal, H. Bualbanat, R. AlRamdan, N. Howarth, P. Parthasarathy, A. AlDarwish, E. Stephenson, Y. Almahanna, M. Hussain, L. A. Diaz, and J. P. Arab, "Modernizing metabolic dysfunction-associated steatotic liver disease diagnostics: the progressive shift from liver biopsy to

noninvasive techniques," *Therapeutic Advances in Gastroenterology*, vol. 17, p. 17562848241276334, 2024.

[8] J. Quek, K. E. Chan, Z. Y. Wong, C. Tan, B. Tan, W. H. Lim, D. J. H. Tan, A. S. P. Tang, P. Tay, J. Xiao, J. N. Yong, R. W. Zeng, N. W. S. Chew, B. Nah, A. Kulkarni, M. S. Siddiqui, Y. Y. Dan, V. W.-S. Wong, M. Noureddin, M. Muthiaht, and C. H. Ng, "Global prevalence of non-alcoholic fatty liver disease and ls ® non-alcoholic steatohepatitis in the overweight and obese o population: a systematic review and meta-analysis," 2022.

[9] D. E. Kleiner, E. M. Brunt, M. V. Natta, C. Behling, M. J. Contos, O. W. Cummings, L. D. Ferrell, Y. Liu, M. S. Torbenson, A. Unalp-Arida, M. Yeh, A. J. McCullough, and A. J. Sanyal, "Design and validation of a histological scoring system for nonalcoholic fatty liver disease†," *Hepatology*, vol. 41, pp. 1313–1321, 6 2005.

[10] J. Frączek, A. Sowa, P. Agopsowicz, M. Migacz, K. Dylińska-Kala, and M. Holecki, "Non-invasive tests as a replacement for liver biopsy in the assessment of masld," 4 2025.

[11] H. Park, E. L. Yoon, M. Kim, J. H. Park, R. Cheung, J. Y. Cho, H. L. Kim, and D. W. Jun, "Cost-effectiveness of advanced hepatic fibrosis screening in individuals with suspected masld identified by serologic noninvasive tests," *Scientific Reports*, vol. 15, 12 2025.

[12] B. Njei, P. Ameyaw, Y. Al-Ajlouni, L.-P. Njei, and S. Boateng, "Diagnosis and management of lean metabolic dysfunction-associated steatotic liver disease (masld): A systematic review," *Cureus*, 10 2024.

[13] Y. X. Zhang, Y. P. Feng, C. L. You, and L. Y. Zhang, "The diagnostic value of mri-pdff in hepatic steatosis of patients with metabolic dysfunction-associated steatotic liver disease: a systematic review and meta-analysis," *BMC Gastroenterology*, vol. 25, 12 2025.

[14] D. T. Fetzer, T. T. Pierce, M. L. Robbin, G. Cloutier, A. Mufti, T. J. Hall, A. Chauhan, R. Kubale, and A. Tang, "Us quantification of liver fat: Past, present, and future," *Radiographics*, vol. 43, 7 2023.

[15] T. Yamaguchi, "Basic concept and clinical applications of quantitative ultrasound (qus) technologies," 10 2021.

[16] X. Q. Li, G. W. Cheng, I. Akiyama, X. J. Huang, J. Liang, L. Y. Xue, Y. Cheng, M. Kudo, and H. Ding, "Attenuation imaging: Diagnostic differences in hepatic

steatosis for chronic hepatitis b vs metabolic dysfunction-associated steatotic liver disease patients," *World Journal of Gastroenterology*, vol. 31, 3 2025.

[17] R. Gao, J. Han, D. Song, P. Wang, H. Chen, H. Shen, and J. Li, "Quantitative assessment of hepatic steatosis by ultrasound-guided attenuation parameter in patients with impaired glucose tolerance," *Insights into Imaging*, vol. 16, 12 2025.

[18] C. Ji, Y. He, Y. Fan, A. Zhu, H. Han, Y. Miao, J. Yu, Y. Shen, S. Chen, Y. Zhu, H. Xu, and H. Yin, "Ultrasound-based fat fraction for detection of hepatic steatosis and quantification of liver fat content using liver biopsy as the reference standard," *European Radiology*, 2025.

[19] S. K. Jeon, J. M. Lee, I. Joo, and S. J. Park, "Quantitative ultrasound radiofrequency data analysis for the assessment of hepatic steatosis in nonalcoholic fatty liver disease using magnetic resonance imaging proton density fat fraction as the reference standard," *Korean journal of radiology*, vol. 22, pp. 1077–1086, 7 2021.

[20] K. Sugimoto, M. Abe, H. Oshiro, H. Takahashi, T. Kakegawa, Y. Tomita, Y. Yoshimasu, H. Takeuchi, and T. Itoi, "The most appropriate region-of-interest position for attenuation coefficient measurement in the evaluation of liver steatosis," *Journal of Medical Ultrasonics*, vol. 48, pp. 615–621, 10 2021.

[21] M. Bi, F. Liu, J. Yu, Y. He, P. Liang, and H. Yang, "Preliminary study on determining the optimal position of region of interest for evaluating hepatic steatosis using ultrasound attenuation imaging," *Abdominal Radiology*, vol. 50, pp. 4380–4388, 9 2025.

[22] G. Ferraioli, A. Raimondi, L. Maiocchi, A. D. Silvestri, G. Poma, V. Kumar, and R. G. Barr, "Liver fat quantification with ultrasound: Depth dependence of attenuation coefficient," *Journal of Ultrasound in Medicine*, vol. 42, pp. 2247–2255, 10 2023.

[23] Y. Fan, K. Chen, Q. Zhao, H. Yin, Y. Zhu, and H. Xu, "Quantitative ultrasound analysis for non-invasive assessment of hepatic steatosis in metabolic dysfunction-associated steatotic liver disease," *Clinical hemorheology and microcirculation*, vol. 89, pp. 251–259, 3 2025.

[24] J. Jamrasnarodom, T. Apiparakoon, S. Marukatat, O. Chaichuen, S. Sukchareon, and R. Chaiteerakij, "Quantitative ultrasound assessment of liver fat using deep learning and clinical data integration," *Journal of Medical and Biological Engineering*, 2025.

[25] Y. Zhu, H. Yin, D. Zhou, Q. Zhao, K. Wang, Y. Fan, K. Chen, H. Han, and H. Xu, "A prospective comparison of three ultrasound-based techniques in quantitative diagnosis of hepatic steatosis in nafld," *Abdominal Radiology*, vol. 49, pp. 81–92, 1 2024.

[26] P. J. Eddowes, M. Sasso, M. Allison, E. Tsochatzis, Q. M. Anstee, D. Sheridan, I. N. Guha, J. F. Cobbold, J. J. Deeks, V. Paradis, P. Bedossa, and P. N. Newsome, "Accuracy of fibroscan controlled attenuation parameter and liver stiffness measurement in assessing steatosis and fibrosis in patients with nonalcoholic fatty liver disease," *Gastroenterology*, vol. 156, pp. 1717–1730, 5 2019.

[27] E. A. Miranda, A. Basarab, and R. Lavarello, "Enhancing ultrasonic attenuation images through multi-frequency coupling with total nuclear variation," *The Journal of the Acoustical Society of America*, vol. 156, pp. 2805–2815, 10 2024.

[28] I. Rafati, F. Destrempes, L. Yazdani, M. Gesnik, A. Tang, and G. Cloutier, "Regularized ultrasound phantom-free local attenuation coefficient slope (acs) imaging in homogeneous and heterogeneous tissues," *IEEE Transactions on Ultrasonics, Ferroelectrics, and Frequency Control*, vol. 69, pp. 3338–3352, 12 2022.

[29] S. Merino and R. Lavarello, "Spatially weighted fidelity and regularization terms for attenuation imaging," *IEEE Transactions on Ultrasonics, Ferroelectrics, and Frequency Control*, vol. 72, pp. 338–350, 2025.

[30] J. Timaná, H. Chahuara, L. Basavarajappa, A. Basarab, K. Hoyt, and R. Lavarello, "Reducing the degrees of freedom for simultaneous estimation of ultrasonic attenuation and backscatter coefficients: Application to liver steatosis detection," in *IEEE International Ultrasonics Symposium, IUS*, IEEE Computer Society, 2023.

[31] J. A. Jensen, *Ultrasound Imaging and Its Modeling*, pp. 135–166. Berlin, Heidelberg: Springer Berlin Heidelberg, 2002.

[32] L. Demi, "Practical guide to ultrasound beam forming: Beam pattern and image reconstruction analysis," 9 2018.

[33] J. Foiret, X. Cai, H. Bendjador, E. Y. Park, A. Kamaya, and K. W. Ferrara, "Improving plane wave ultrasound imaging through real-time beamformation across multiple arrays," *Scientific Reports*, vol. 12, 12 2022.

[34] R. Ali, T. Mitcham, L. Brickson, W. Hu, M. Doyley, D. Rubens, Z. Ignjatovic, N. Duric, and J. Dahl, "Separation of mainlobe and sidelobe contributions to b-mode ultrasound images based on the aperture spectrum," *Journal of Medical Imaging*, vol. 9, 1 2022.

[35] Verasonics Inc., *Vantage® NXT System User Manual*. Verasonics Inc., Kirkland, WA, USA, 2025. Document ID D00107, Revision H.

[36] Verasonics Inc., *Vantage® NXT Sequence Programming Manual*. Verasonics Inc., Kirkland, WA, USA, 2024. Document ID D00163, Revision H.

[37] T. L. Szabo and P. A. Lewin, "Ultrasound transducer selection in clinical imaging practice," *Journal of Ultrasound in Medicine*, vol. 32, pp. 573–582, 4 2013.

[38] T. N. Nguyen, A. J. Tam, M. N. Do, and M. L. Oelze, "Estimation of backscatter coefficients using an in situ calibration source," *IEEE Transactions on Ultrasonics, Ferroelectrics, and Frequency Control*, vol. 67, pp. 308–317, 2 2020.

[39] G. Ghoshal and M. L. Oelze, "Time domain attenuation estimation method from ultrasonic backscattered signals," *The Journal of the Acoustical Society of America*, vol. 132, pp. 533–543, 7 2012.

[40] E. L. Madsen, G. R. Frank, and T. A. Hobson, "Multi-imaging modality tissue mimicking material and phantom." U.S. Patent 6 318 146, Nov. 2001. Granted Nov. 20, 2001.

[41] E. L. Madsen, F. Dong, G. R. Frank, B. S. Garra, K. A. Wear, T. Wilson, J. A. Zagzebski, H. L. Miller, K. K. Shung, S. H. Wang, E. J. Feleppa, T. Liu, W. D. O'Brien, K. A. Topp, N. T. Sanghvi, A. V. Zaitsev, T. J. Hall, J. B. Fowlkes, O. D. Kripfgans, and J. G. Miller, "Interlaboratory comparison of ultrasonic backscatter, attenuation, and speed measurements," *Journal of Ultrasound in Medicine*, vol. 18, pp. 615–631, 1999.

[42] J.-F. Chen, J. A. Zagzebski, S. Member, and E. L. Madsen, "Tests of backscatter coefficient measurement using broadband pulses," tech. rep., 1993.

[43] N. Bottenus, "Recovery of the complete data set from focused transmit beams," *IEEE Transactions on Ultrasonics, Ferroelectrics, and Frequency Control*, vol. 65, pp. 30–38, 1 2018.

[44] R. Ali, C. D. Herickhoff, D. Hyun, J. J. Dahl, and N. Bottenus, "Extending retrospective encoding for robust recovery of the multistatic data set," *IEEE Transactions on Ultrasonics, Ferroelectrics, and Frequency Control*, vol. 67, pp. 943–956, 5 2020.

[45] W. Simson, L. Zhuang, S. J. Sanabria, N. Antil, J. J. Dahl, and D. Hyun, "Differentiable beamforming for ultrasound autofocusing," in *Medical Image Computing and Computer Assisted Intervention – MICCAI 2023* (H. Greenspan, A. Madabhushi, P. Mousavi, S. Salcudean, J. Duncan, T. Syeda-Mahmood, and R. Taylor, eds.), (Cham), pp. 428–437, Springer Nature Switzerland, 2023.

[46] S. A. Julious, "Sample size of 12 per group rule of thumb for a pilot study," *Pharmaceutical Statistics*, vol. 4, pp. 287–291, 10 2005.

[47] A. L. Whitehead, S. A. Julious, C. L. Cooper, and M. J. Campbell, "Estimating the sample size for a pilot randomised trial to minimise the overall trial sample size for the external pilot and main trial for a continuous outcome variable," *Statistical Methods in Medical Research*, vol. 25, pp. 1057–1073, 6 2016.

[48] F. Deeba, C. Schneider, S. Mohammed, M. Honarvar, E. Tam, S. Salcudean, and R. Rohling, "Swtv-ace: Spatially weighted regularization based attenuation coefficient estimation method for hepatic steatosis detection," in *Lecture Notes in Computer Science (including subseries Lecture Notes in Artificial Intelligence and Lecture Notes in Bioinformatics)*, vol. 11768 LNCS, pp. 610–618, Springer Science and Business Media Deutschland GmbH, 2019.

[49] M. L. Oelze and W. D. O'Brien, "Defining optimal axial and lateral resolution for estimating scatterer properties from volumes using ultrasound backscatter," *The Journal of the Acoustical Society of America*, vol. 115, pp. 3226–3234, 6 2004.

[50] J. Ormachea and K. J. Parker, "A preliminary study of liver fat quantification using reported ultrasound speed of sound and attenuation parameters," *Ultrasound in Medicine and Biology*, vol. 48, pp. 675–684, 4 2022.

[51] P. K. Hsu, L. S. Wu, H. H. Yen, H. P. Huang, Y. Y. Chen, P. Y. Su, and W. W. Su, "Attenuation imaging with ultrasound as a novel evaluation method for liver steatosis," *Journal of Clinical Medicine*, vol. 10, pp. 1–9, 3 2021.